Scripps Institution of Oceanography
University of California, San Diego.
La Jolla, California 92093

Quasi-Lagrangian Measurements of Microstructure and Shear Near a Front in the Coastal California Thermocline

Timothy F. Duda and Charles S. Cox

Research Sponsored by the Office of Naval Research

August 1988

SIO Reference No. 88-15

1. Introduction

For over a decade measurements of temperature and velocity fluctuations at wavelengths influenced by molecular diffusion have been studied in an effort to understand vertical turbulent diffusion of heat in the upper 600 meters of the ocean. In upper-ocean regions not characterized by special circumstances like double-diffusion or persistent high shear (such as the equatorial undercurrent), measurements in the stratified region below the mixed layer have indicated vertical eddy thermal diffusivity κ_e a factor of 3 to 10 lower than the 10^{-4} $m^2 s^{-1}$ value suggested by the advection-diffusion model of Munk (1966) (Elliot and Oakey, 1980; Gregg, 1977; Gregg et al., 1986; Moum and Osborn, 1986). Aside from recent confusion over double-diffusive flux (e.g. Kunze, 1987) a succession of studies have qualitatively illustrated an association between kinetic energy dissipation and κ_e. At molecular diffusion scales, velocity and temperature fluctuations seem related (Oakey, 1985; Gregg et al., 1986), coinciding with the expectation that dissipation of kinetic energy is directly influential on events contributing to κ_e. At larger scales from which energy is supplied, Gregg et al. (1986) have observed a correlation between fine scale shear from near-inertial motion and persistent patches of microscale activity, Marmorino et al. (1985) have observed a correlation between fine scale temperature fluctuations and fine scale shear intensity, and Marmorino (1987b) has seen indications of shear instability.

The California current region of swirls, eddys, upwelling and squirts is suited to studies of microstructure and vertical mixing because many different situations exist, including some with double-diffusive flux and some influenced by bottom topography. In the main thermocline in 300 meter deep water Washburn (1987) has recorded high levels of microstructure, while at a location 400 km SW of San Diego Gregg et al. (1986) have recorded lower levels reminiscent of those from the open ocean. Both of those studies involved repeated profiles of temperature microstructure. We present similar data from two regions. We emphasize data from one region, in part because profiles of vertical velocity were concurrently collected.

The emphasized region was of abyssal depth, was 100 km from the coast, and was in an offshore jet of amplitude 0.2 $m s^{-1}$ near a temperature front extending over 250 meters below the surface. This region shared with Washburn's (1987) region the characteristic of strong mesoscale flow influenced by the coast, but shared with Gregg et al.'s (1986) region the absence of the immediate influence of bottom topography. In this region, the mean dissipation rate of thermal variance χ_T and our estimate of κ_e, were between those of an active portion of Washburn's data and those of Gregg et al. At this location we found persistent microstructure activity on one side of a surface temperature front and sporadic activity on the other. Vertical shear was not statistically different on the two sides and no persistent shear was associated with the persistent microstructure, so one may infer that the persistent high χ_T marked regions especially prone to double-diffusive activity, although the persistent patch positions did not

correspond well with temperature inversions which indicate intrusion. Characteristics of the sporadic microstructure on the other side of the front agree with the model of internal-wave dissipation of Henyey, Wright and Flatté (1986), and with previous estimates of turbulent vertical flux.

Observations of microstructure from the other region, much further offshore in water not directly influenced by coastal upwelling, are presented because they contain the thinnest, most long-lived patches, reminiscent of the structures observed by Yamazaki and Lueck (1987).

Data consist of profiles of temperature gradient variance (TGV), temperature, and horizontal velocity collected at 0.005 megapascal ($\approx$ 0.5 m) intervals below the surface mixed layer at pressures less than 3.0 MPa (1 MPa is the pressure at roughly 100 m depth). These profiles were collected with the Cartesian Diver free vehicle (Duda, Cox and Deaton, 1987), which remained confined to a limited volume of water during the three day-long sampling periods. This Lagrangian character allows sampling of fields more statistically homogeneous than does most ship-bourne sampling, although the experiment of Gregg et al. followed a drogued buoy with a similar effect. TGV was estimated from a high resolution conductivity measurement. For wavelengths greater than 5 millimeters, the conductivity gradient can be a good proxy for temperature gradient in the upper ocean. Resulting from the analysis of TGV are estimates of mean χ_T and variability of χ_T. Variations between these characteristics in 40-meter depth layers and time-depth maps of χ_T are shown in section 5. Mean vertical turbulent heat flux and a table of average Richardson numbers are given in sections 6 and 7 for the emphasized region of sporadic (possibly virtually entirely turbulent) microstructure.

2. Instrumentation and data processing

The Cartesian Diver drifter (Duda, Cox and Deaton, 1987) is programmable, and can collect continuously repeated profiles in the upper 350 m of the ocean by adjusting its volume at either end of preset pressure ranges. A round-trip between 25 and 300 meters depth is completed in approximately 1 hour. Baroclinic velocity $U(z)$ of vertical wavelength greater than 10 meters is measured using the technique of geomagnetic induction, with a sampling interval of 0.5 meter (sampling rate one-quarter hertz) and with resolution of fluctuations of 10 meters or greater wavelength. Profiles of temperature $T(z)$ are measured using an alloy resistance sensor, at the same sampling interval. While this sampling interval is adequate to resolve internal-wave scale velocity structure, temperature (and conductivity, which can also be recorded) is not well enough resolved to investige double-diffusion and intrusion.

The microconductivity signal is from an a sensor mounted on one wing 0.3 meters off the vertical rotation axis of the Diver, which spins as it profiles. The sensor has a speed through the water between 0.15 and 0.2 m s^{-1} and moves in a helical trajectory

with inclination roughly 45 degrees from the horizontal, so it is sensitive to both vertical and horizontal fluctuations. The sensor, described in more detail by Washburn and Deaton (1986) and Duda et al. (1987), is a four-electrode type, has an open cell, and has a low-pass response with half-power point of 100 cycles per meter at flow rate 0.44 $m\,s^{-1}$. Analog circuitry differentiates the conductivity time series then produces six bandpassed channels, evenly spaced in a geometric ratio and extending over the band [0.5-32] Hz. This is equivalent to a wavenumber band of [3-200] cpm for 0.16 $m\ s^{-1}$ probe speed. The bandpassed signals are rectified to give average amplitude levels, which are sampled and recorded at one-quarter Hz, matching the sampling rate of $U(z)$ and $T(z)$. Power spectral estimates are computed from the average amplitudes, after recovery, as in Duda et al. Fig. 1 shows four conductivity gradient spectra from the Cμ1 deployment, illustrating both the broad dynamic range of the measurement and variability of the spectral peak wavenumber.

An estimate of system noise can be derived from the temporal variation of the average amplitudes. Approximately 20 percent of the spectra from the Cμ1 and Cμ2 deployments (section 3) lie near a minimum (Fig. 1), possibly associated with an instrument noise threshold level. This level of 4×10^{-6} (siemens m^{-2})^2 is 10 times the laboratory estimate of noise introduced by the driver and amplifier circuitry alone, without the bandpass circuitry. The estimates of amplitude threshold levels are affected by voltage offsets in the filters and rectifiers, which may have varied in an unknown fashion while the Diver was cycling through water of 9 to 16 °C. The minimum variance was a factor of two higher for the Bμ1 data set due to a noisy probe connection.

Fig. 2 shows four consecutive profiles of one-dimensional conductivity gradient variance (CGV), $<(\partial\sigma/\partial z)^2>$, and conductivity spectral peak location. The brackets indicate an average over a meter-scale depth range. In the theory of the spatial spectrum of a passive scalar (with a diffusivity much greater than the kinematic viscosity) carried by homogeneous isotropic turbulence (Batchelor, 1959), the spectrum of a scalar gradient (which temperature approximates) is peaked. The position of the peak is a function of ϵ, the rate of turbulent kinetic energy dissipation. This is because fluctuations of any passive scalar can exist at small scale, despite molecular diffusion, at high rates of production and dissipation of turbulent kinetic energy, whereas they cannot for low rates of energy dissipation. Conductivity is a function of both temperature T and salinity S, with S less diffusive than T, so the spectral peak location does not always provide a reliable estimate of ϵ (example spectra are shown in the Appendix).

We assume constant salinity for wavenumbers greater than 3 cpm and convert CGV to TGV using the factor (approximated as constant) 0.089 $S\,m^{-1}K^{-1}$ (Washburn and Gibson, 1982). The accuracy of this conversion is addressed in the Appendix. The largest errors occur in water masses with $\Delta T/\Delta S$ between -2 and 2, particularly at low kinetic energy dissipation rate. Most individual 0.005 MPa samples of TGV are accurate within a factor of 1.5, and the errors from the others should not affect the qualitative results of this work.

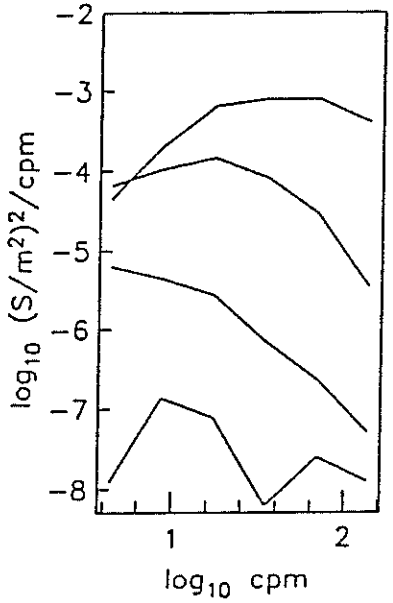

Figure 1. Conductivity gradient power spectral estimates taken from the $C\mu 1$ experiment, in the [3-200] cpm band. The spectra are from four unrelated 0.5 m depth ranges, and are chosen to show the dynamic range of the measurement. The lowest spectrum is near the noise level and has variance $4.5 \times 10^{-6}(\mathrm{S\ m^{-2}})^2$. The others have variances 1.1×10^{-4}, 6.5×10^{-3}, and 1.1×10^{-1}, with the last being among the highest measured. A correlation of high variance with peak at high wavenumber is seen. This is in agreement with Batchelor's (1959) theory for situations where conductivity fluctuations are almost entirely due to temperature, with salinity influence minimal.

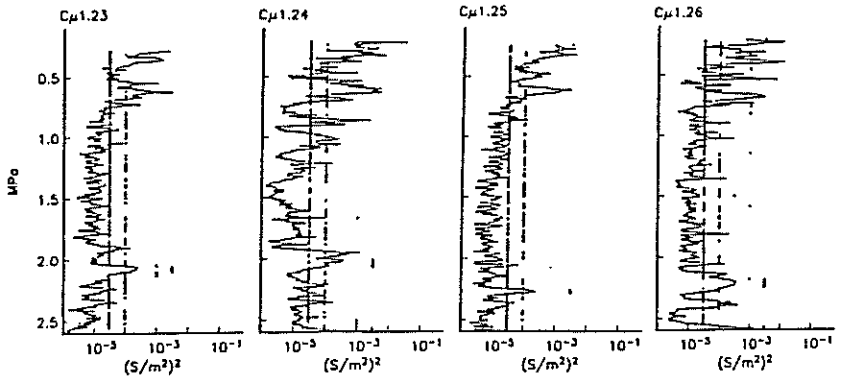

Figure 2. Four consecutive microscale conductivity gradient variance profiles, with an overlay of dots showing peak location profiles (peak location is indicated only when the variance is well above the noise level). Dots further to the right indicate peak location at higher wavenumbers. The dots at 3×10^{-5} indicate spectral peak at [6-12] cpm, dots at 10^{-4} indicate peak at [12-24] cpm, and so on, with dot at 3×10^{-3} indicating peak at [100-200] cpm (spectral peak unresolved). Any peak at [3-6] cpm is disregarded. Note the appearance four consecutive times (profiling down, up, down, and up) of a high wavenumber peak between 2.0 and 2.3 MPa.

Mean levels and variances of TGV were calculated for 0.4 MPa pressure ranges beneath the surface mixed layer. The rate of dissipation of temperature fluctuations, χ_T, is approximately related to one-dimensional TGV by

$$\chi_T = 6\kappa_T < (\partial T'/\partial z)^2 > \quad . \tag{1}$$

where κ_T is the molecular coefficient of thermal diffusivity, taken to be $1.4 \times 10^{-7} m^2 s^{-1}$, and temperature structure is composed of mean and fluctuating components: $T(z,t) = T_0(z) + T'(z,t)$; $< T' > \equiv 0$. Isotropy of temperature fluctuation intensity has been assumed, so this is an upper-bound estimate of χ_T from the one-dimensional data. Values of CGV in $(S\ m^{-2})^2$ can be converted to χ_T (units $K^2 s^{-1}$) by multiplying by 1.06×10^{-4}, while TGV in $(K\ m^{-1})^2$ can be converted to χ_T by multiplying by 8.4×10^{-7}.

3. Deployments

The data are divided into three sets, each sampled from within a confined volume of water (see section 4). Two sets, coded Cμ1 and Cμ2, consisting each of 16 hourly TGV profiles between 0.3 and 2.5 MPa pressure, were collected 10-12 August 1984 on either side of a surface temperature front 100 km WSW of Pt. Buchon, near San Luis Obispo, CA. This central California region is characterized by coastal upwelling, jets and eddies (e.g. Kosro and Huyer, 1986). The Cμ1 profiles were collected on the cold (south) side of the front, surface temperature 16.9°, while the Cμ2 profiles were collected on the other side, with surface temperature 17.5°. The Diver was advected to the west at the average rate of 0.2 $m\ s^{-1}$ during these deployments, Fig. 3, so this front was associated with an offshore jet. The third set, included for comparison, consists of 11 hourly TGV profiles between 0.3 to 3.0 MPa, collected during August 1985 at an open ocean location 28° N, 122° W, 360 km southeast of San Diego, and is indicated by the code Bμ1 (B is mnemonic for Baja California).

Fig. 4 shows mean temperature profiles at depths of interest for the three data sets. Individual profiles (Fig. 5) show unique fine structures over scales of a few meters and exhibit internal wave straining, but were otherwise uniform for the duration of each deployment. The C profiles of Fig. 5 show temperature inversions, indicating interleaving and intrusion.

Clouds persisted throughout the C experiment, preventing satellite imaging of the front and jet. During the Cμ1 deployment of August 10 wind was from the northwest at 3-5 knots. During the Cμ2 deployment of August 11-12, the wind was from the northwest at 13 knots at launch and 15-20 knots for the duration. Wind was from the west at 5-8 knots for the Bμ1 deployment, with clear skies.

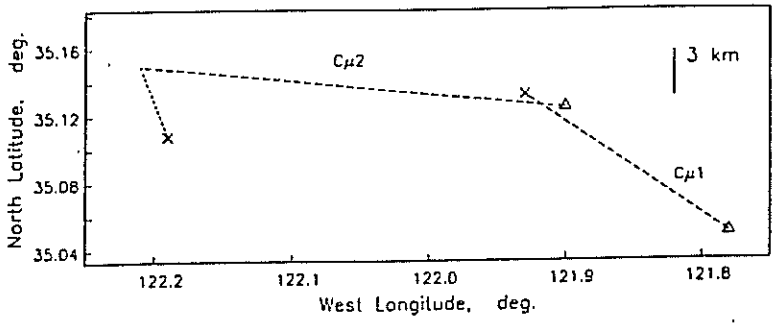

Figure 3. Map showing the launch locations (Δ) and recovery locations ($\times$) for the central coast frontal deployments. The long-dashed lines indicate approximate mean advection of the diver, which was 16 km total at the rate of 0.16 $m\,s^{-1}$ during Cμ1, and 28 km at 0.24 $m\,s^{-1}$ during Cμ2. Only data from the first 16 hours of each deployment were reliable, corresponding to the right-hand portions of the tracks.

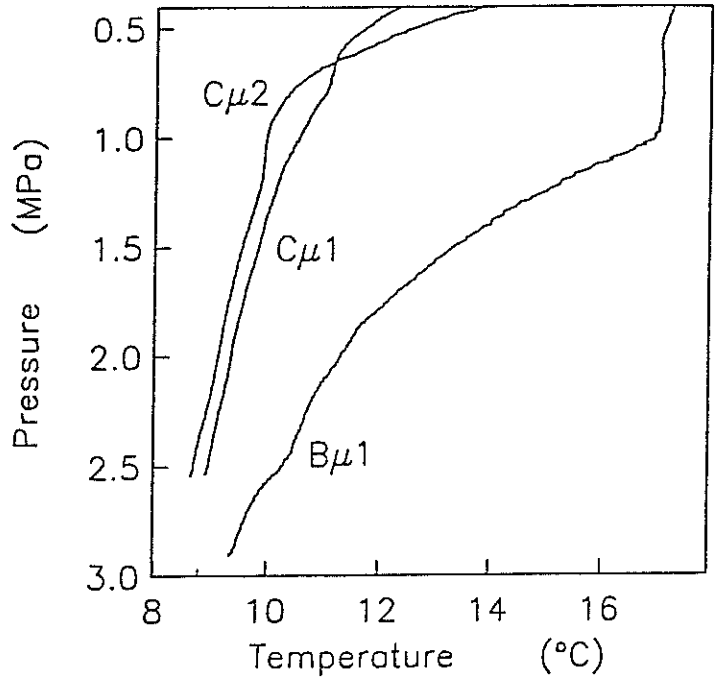

Figure 4. Average temperature profiles $T_0(z)$ for the three deployments. The profiles were calculated by averaging all T recorded at a specific pressure, eliminating persistent fine structure. Remnants of a surface mixing layer extend to 1.0 MPa in Bμ1.

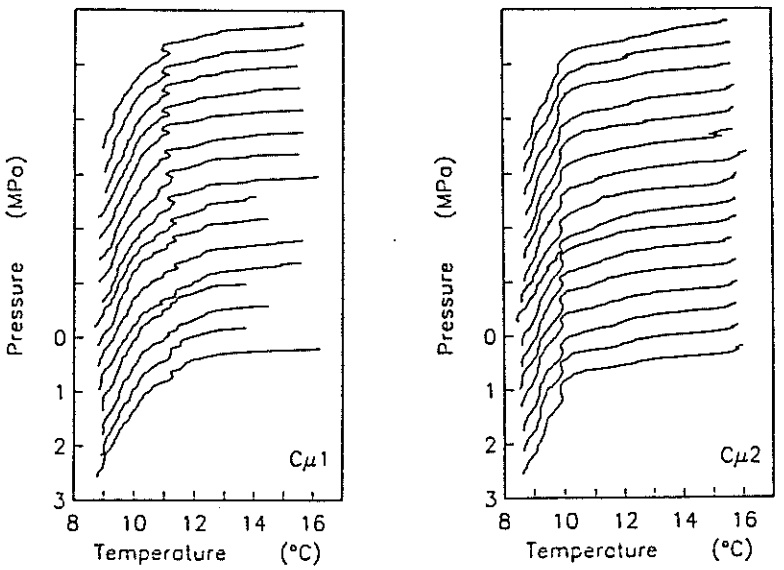

Figure 5. Hourly temperature profiles from the C (frontal) experiments, offset 0.4 MPa vertically. Temperature inversions can be seen near 0.7 MPa during Cμ1 and from 1.0 to 1.2 MPa during Cμ2. Isotherm depths taken from these profiles are shown in Figure 6.

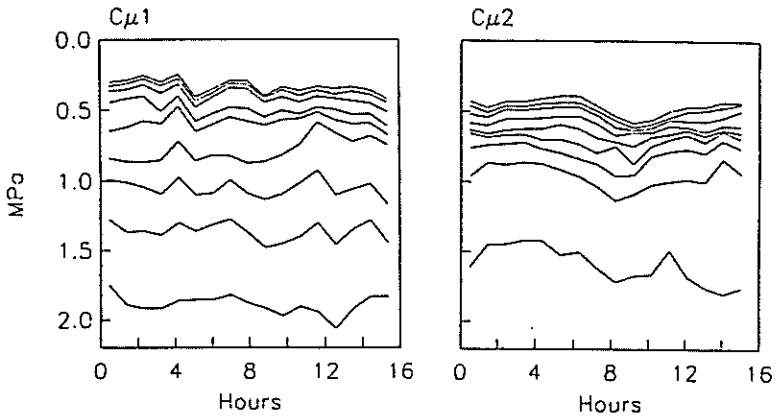

Figure 6. Depths of 13.5° to 9.5° isotherms throughout the two C (frontal) deployment periods. The instrument remained in each of two recognizable water masses for the duration of each period.

4. Lagrangian character of the sampling

The profiling of the instrument through the vertically structured velocity field causes the size of the water mass within which the Diver has sampled to grow with time. Nonetheless, temperature data from the frontal (C) data sets (Fig. 6) shows uniformity of sampled isotherm depths throughout each deployment, with unique gross temperature structure for each deployment. This indicates that the Diver remained in separate volumes of water throughout each deployment.

Since the baroclinic component of velocity has been measured, Fig. 7, the size of these volumes can be estimated. The horizontal advection (relative to the unknown time-dependent barotropic flow) of isothermal surfaces can be calculated from the hourly velocity measurements, assuming a horizontal coherence length of velocity of a few kilometers. Since the Cartesian Diver actually measures its own baroclinic velocity, an integration of all measured velocities gives the advection of the Diver. Figs. 8a and 9a show baroclinic horizontal advection of the 9.5° isotherm, the 11° isotherm, and the Diver. Figs. 8b and 9b show hourly Cartesian Diver position relative to the position of the 9.5 and 11° parcels it sampled on the initial profiles. Under the assumption that dispersion is similar for all depths, simply enclosing the position tracks in a circle gives an estimate of the area sampled by the Diver, about 9 km^2 each 16 hour period. Another way to calculate this is to note that the mean displacement from the initially sampled parcel after 16 hours is 1.7 km (taken from the four tracks shown in Figs. 8b and 9b), which is the radius of a 9 km^2 circle. Barotropic velocities should be smooth over the spatial scales of a few kilometers and should not effect this estimate.

The dispersion of Diver position relative to a parcel of water (Figs. 8b and 9b) is reminiscent of the theoretical random walk process. The dispersion of the Diver, however, exhibits some continuity of direction between successive steps, with changing step length, rather than constant step length and uncorrelated direction.

5. Mean and variance of dissipation rate χ_T

Mean values and moments of quantities having probability distributions with extended tails are difficult to estimate with finite sampling. Baker and Gibson (1987) discuss the calculation of mean ocean microstructure levels using the special maximum-likelihood estimator for the log-normal distribution, which χ_T and energy dissipation rate ϵ fit somewhat (Washburn and Gibson, 1984, Osborn and Lueck, 1985; Gregg et al. 1986; Baker and Gibson, 1987). For small data sets they show that this estimator will give higher mean estimates than the sample mean (the normalized sum of all sample values). However, for large numbers of independent samples the sample mean is a good estimator of the mean for any distribution. Gregg et al. (1986) show agreement between the maximum-likelihood mean and the sample mean for a large microstructure data set from the ocean.

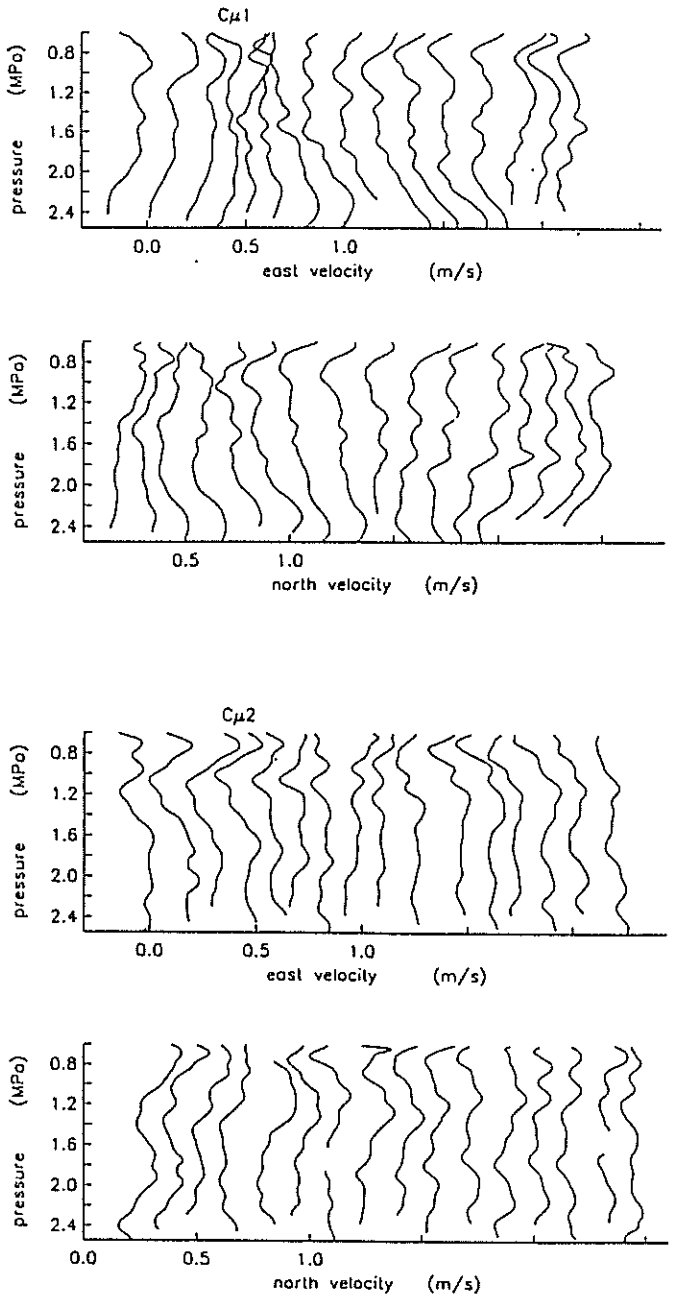

Figure 7. Velocity profiles for Cμ1,2. These are from Cartesian diver ascents only, and were taken approximately hourly. Velocity has been block averaged over 10 meters vertically to eliminate electrode noise. The offset is 0.15 m s^{-1} for each successive profile.

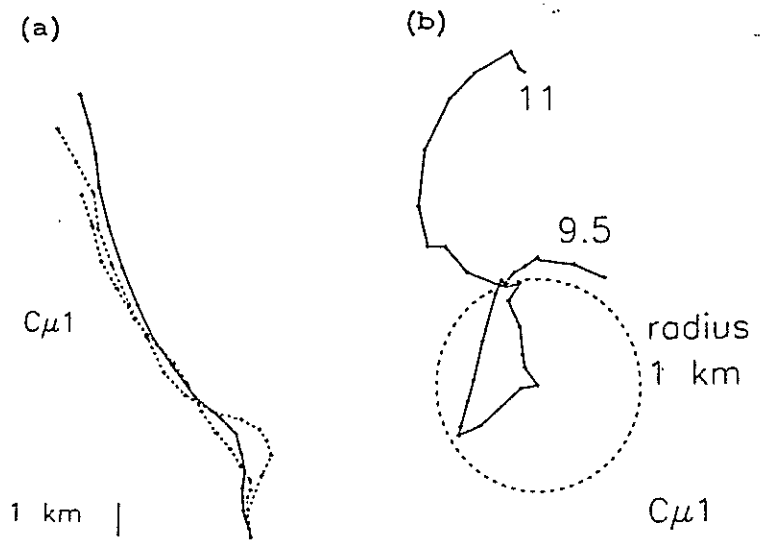

Figure 8. Drift tracks calculated using baroclinic velocities recorded by the diver during the Cμ1 deployment. The +' s mark hourly intervals. The solid line in (a) is the diver track, the dashed lines are approximate tracks of the water parcels at 9.5° and 11° which the diver passed through on the first drop. Velocities of the diver were recorded continuously, while the parcel velocities were recorded hourly as the diver passed that isotherm. (b) shows hourly diver positions relative to the parcel positions, computed by subtracting tracks of (a).

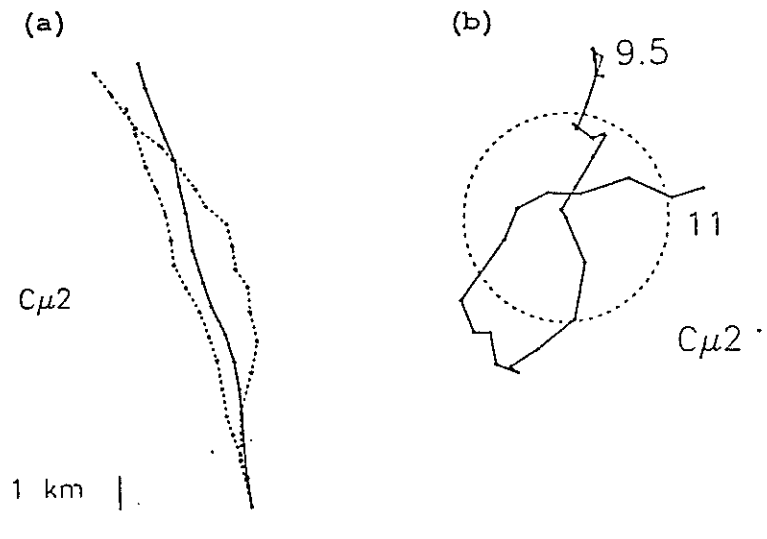

Figure 9. Same as Figure 8, but for the Cμ2 deployment.

The Cartesian Diver data sets are also large enough that the unbiased sample mean $\overline{\chi}_{sm}$ is similar to the biased maximum-likelihood mean $\overline{\chi}_{mle}=\overline{\chi}_{sm}\exp(\mu + V/2)$, where μ is the mean natural logarithm of a log-normal distribution fitted to the distribution of the dimensionless variable $\chi_T/\overline{\chi}_{sm}$, V is the variance of the natural logarithms of that fitted distribution, and the overline indicates an average over time and space. Gibson (1987) and Baker and Gibson (1987) call V the intermittency factor. If χ_T were truly log-normal, the variance of the estimate $\overline{\chi}_{mle}$ would decrease for an increasing number of samples. However, the true distribution may differ. Gregg et al. (1986) point out that increasing the amount of data used in determining average ocean dissipation rates may not result in improved estimates, due to nonstationarity over the time and space scales of a typical experiment.

Confidence intervals for $\overline{\chi}_{sm}$ are difficult to estimate because the distributions are not normal and the variance is not well known. Baker and Gibson (1987) have calculated confidence intervals for $\overline{\chi}_{mle}$ assuming the true distribution is log-normal. If all χ_T samples are assumed to be independent, the 95% confidence intervals on $\overline{\chi}_{mle}$ are from 0.79 to 1.26 times each estimate. If only one in four samples is assumed to be independent, these become 0.63 to 1.59. Log-variance V calculated using the maximum-likelihood procedure is a useful indicator of the variability of χ_T, because of the skewed shape of the non-normal pdf's and the threshold level which may have been determined by the instrumentation.

We calculated $\overline{\chi}_{sm}$, $\overline{\chi}_{mle}$ and V as functions of depth individually for the three data sets (Table 1). We found no systematic difference between $\overline{\chi}_{sm}$ and $\overline{\chi}_{mle}$. Only the profiles taken while the instrument was falling were used since the noise level was slightly higher while the instrument was rising. In addition, the data were edited to exclude signals of continuous high level extending 50 meters or more, indicating fouling of the probe, about 20 percent of the data. Individual probability distribution functions (pdf's) were examined for 0.4 MPa pressure ranges to avoid the problem of nonstationarity with depth and to preserve any depth variation. Fig. 10 shows example pdf's from the three deployments. The Cμ1 example shows significant departure from log-normality, possibly associated with intrusion and conditions favorable for double-diffusive activity, discussed in the Appendix.

An associated dimensionless parameter calculated for 0.4 MPa intervals is

$$C \equiv \frac{3\overline{<(\partial T'/\partial z)^2>}}{(\partial T_0/\partial z)^2} \quad . \tag{2}$$

This is an estimate of the parameter

$$C_T \equiv \frac{\overline{<(\nabla T')^2>}}{(\partial T_0/\partial z + \Gamma)^2} \equiv \frac{\overline{\chi}_T}{2\kappa_T(\partial T_0/\partial z + \Gamma)^2} \quad , \tag{3}$$

which is discussed in section 6, where Γ is the adiabatic lapse rate of temperature, which is negligible in the upper ocean. The factor of 3 for assumed isotropy of

Table 1. Measured parameters for central California (C) and Baja California (B) data sets. Listed are: mean vertical temperature gradients; sample mean dissipation $\overline{\chi}_{sm}$ and associated parameter C_{sm}; log-normal maximum-likelihood dissipation mean $\overline{\chi}_{mlr}$ and associated C_{mlr}; and log-normal maximum-likelihood variance V.

set	pressure	$\partial T_0/\partial z \times 10^3$	$\overline{\chi}_{sm} \times 10^9$	C_{sm}	$\overline{\chi}_{mlr} \times 10^9$	C_{mlr}	V
	MPa	K m^{-1}	K^{2}sec^{-1}		K^{2}sec^{-1}		nat. log.
Cμ1	0.6-1.0	21	23	186	25	202	3.0
	1.0-1.4	15	6.6	105	-	-	-
	1.4-1.8	11	4.7	139	3.5	103	2.1
	1.8-2.2	9.2	25	1050	5.4	228	4.1
Cμ2	0.6-1.0	50	18	26	212	303	9.2
	1.0-1.4	8.0	4.8	268	8.0	446	7.3
	1.4-1.8	9.0	1.8	79	3.1	137	4.0
	1.8-2.2	9.0	2.0	88	2.4	106	7.7
Bμ1	1.0-1.4	88			60	28	2.5
	1.4-1.8	52			30	40	3.1
	1.8-2.2	29			3.7	16	2.0
	2.2-2.6	24			63	390	5.4

Table 2. Mean dissipation $\overline{\chi}_T$, variance V and mean C observed in the upper ocean. Maximum-likelihood estimates are indicated by the subscript m. The lower reference of a pair is a reanalyses by later authors. All values have been adjusted to give C and $\dot{\chi}_T$ calculated under the assumption of isotropic fluctuations. Refer to Table 1 for our values.

experiment	$\partial T_0/\partial z \times 10^3$	$\overline{\chi}_T \times 10^9$	V	C
	K m^{-1}	K^{2}sec^{-1}	nat. log.	
Gregg (1977, shallow)	31	5.6		21
Gargett (1984)		11		42
Gregg (1977, deep)	3.7	0.7		180
Gargett (1984)		1.4		360
Elliot and Oakey (1979)		22		
Baker and Gibson (1987)		34_m	4.6_m	
Washburn and Gibson (1984)	300	1100_m	5.3_m	
Gregg et al. (1986)	41	11_m	7.0_m	23_m
		11		23
Dillon and Park (1987, shallow)	≈750			160
Dillon and Park (1987, deep)	≈230			278
Washburn (1987)	77	2200		1440

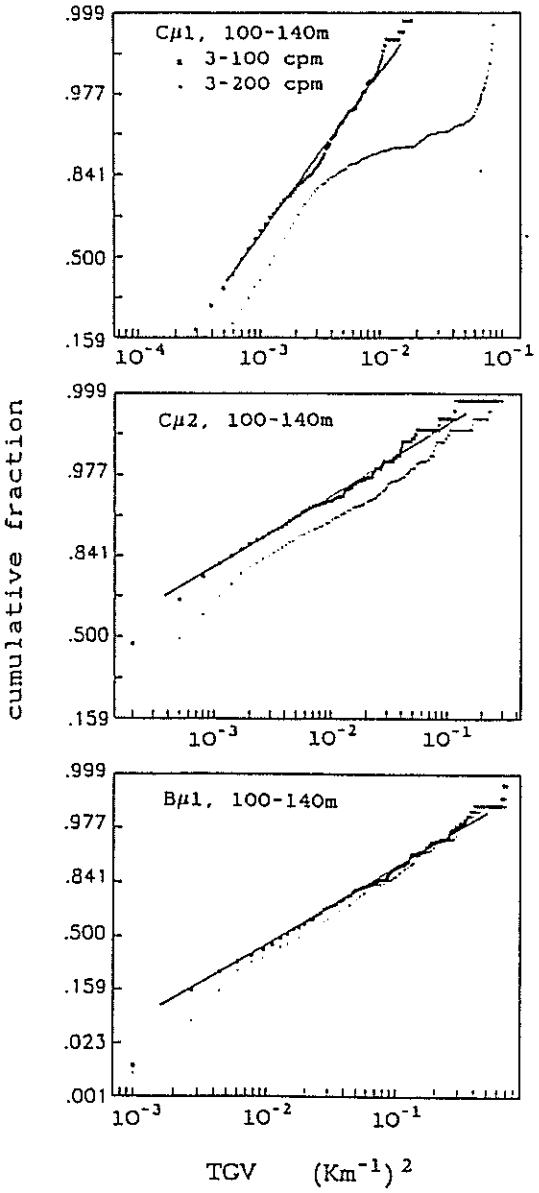

Figure 10. Example empirical-theoretical quantile-quantile plots of temperature gradient variance, with fitted log-normal distributions (solid lines). Log-normally distributed data produce straight lines in this normalized representation of the probability distribution function. Data from three experiments shown, with both [3-100] cpm and [3-200] cpm variance pdf's shown. The Cμ1 [3-200] cpm curve indicates a large number of very high values which may be due to a particularly high level of salinity fluctuations. We analyze pdf's fit to the [3-200] cpm functions, although example fits to the [3-100] cpm functions are shown.

microstructure makes this an upper-bound estimate of C_T in the stratified upper ocean. Values of $\partial T_0/\partial z$ were determined graphically from Fig. 4 and are listed in Table 1, along with C. If all depth regions and all three deployments are weighted equally, the average C_{sm} is 242, while the average C_{mle} is 181.

The individual V from our three deployments varied widely, Fig. 11. Values of V were consistently lower in Cμ1 than in Cμ2, while C varied irregularly. The low average V =3.0 for χ_T from Cμ1 has not been reported previously in the thermocline, although Osborn and Lueck (1985) reported $V \approx 2$ for ϵ from limited regions. The Bμ1 data set has been included primarily because it also has low V, boosting confidence in the Cμ1 values.

Table 2 shows temperature microstructure parameters from various studies. Baker and Gibson (1987) calculated V for the data of Elliot and Oakey (1979) from the GATE experiment, from a large 35-125 m depth range. Washburn and Gibson (1984) calculated V at the mixed-layer base during MILE from 4700 meters of towed microscale conductivity data. Gregg's (1977) data are from the mid-Pacific and are divided into two groups, as in reanalysis by Gargett (1984), those from 2 to 6 MPa and those from 8 to 12 MPa, with each region having a relatively constant mean vertical temperature gradient. Gregg did not include the factor of 3 for isotropy; we have applied that factor to his original data for comparison with the other data sets. Gargett boosted Gregg's figures to account for thermistor response. Gregg et al. (1986) reported V and $\overline{\chi}_T$ for 11 300 samples (at interval 0.005 MPa) taken between 1.4 and 2.0 MPa in the California current. The data of Dillon and Park (1987) are from the seasonal thermocline at 50 °N, 145 °W during the MILE investigation. Data of Washburn (1987) are from south of Santa Cruz Island, California, in an area of 150 to 370 meters depth. Undoubtedly V for temperature microstructure from the persistent turbulent layers of Yamazaki and Lueck (1986) would be low, but was not reported.

The depth-time character of both low and high V situations is shown in Fig. 12. One-half meter samples of χ_T are presented, rather than contours of smoothed χ_T, in order to retain single-point high χ_T events. The low V situations in Cμ1 and Bμ1 exhibit layers of temperature microstructure persistent for hours, similar to those reported by Yamazaki and Lueck (1987). These structures were called patches in the study of Gregg et al. (1986), while they called thinner, short-lived active regions puffs. Puffs are evident in all three volumes (Fig. 12), while patches are missing from Cμ2. Puffs fit the kinematic model of Desaubies and Smith (1982) relating randomly occurring intense internal-wave shear to mixing events, but patches do not. Gregg et al. found that thick and persistent patches contributed more to total mixing than thin brief puffs. Their patches seemed related to persistent inertial shear, but ours were not, based on the concurrent shear observations.

We propose three explanations for the persistent patches. It is likely that our patches were sustained by various mechanisms, since none of the explanations are

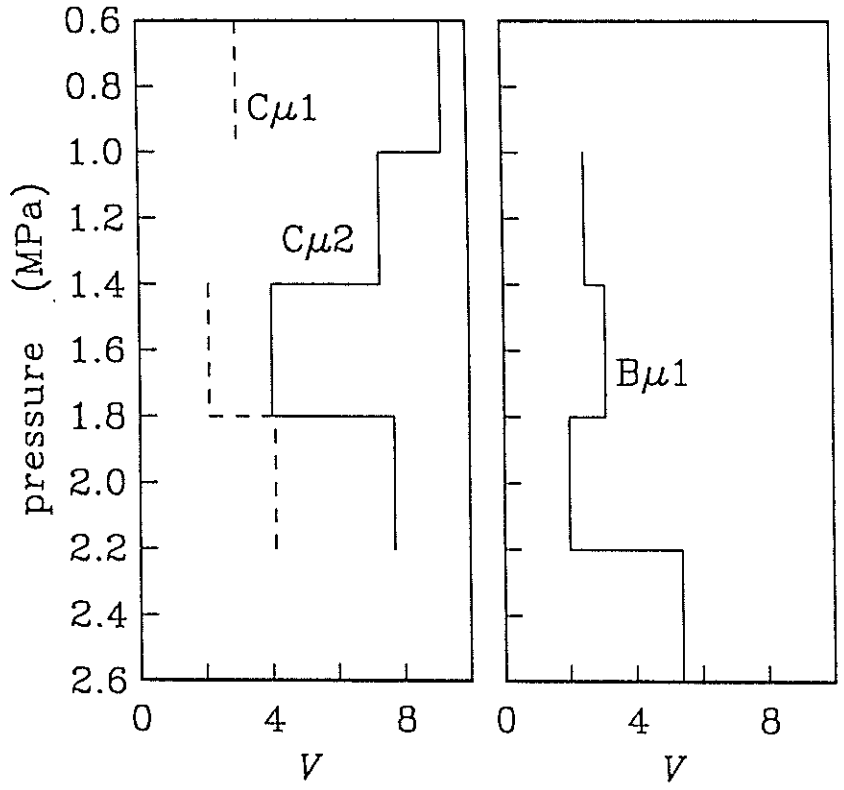

Figure 11. Variances of the logarithm of fitted log-normal distributions, V, for three experiments, as a function of pressure.

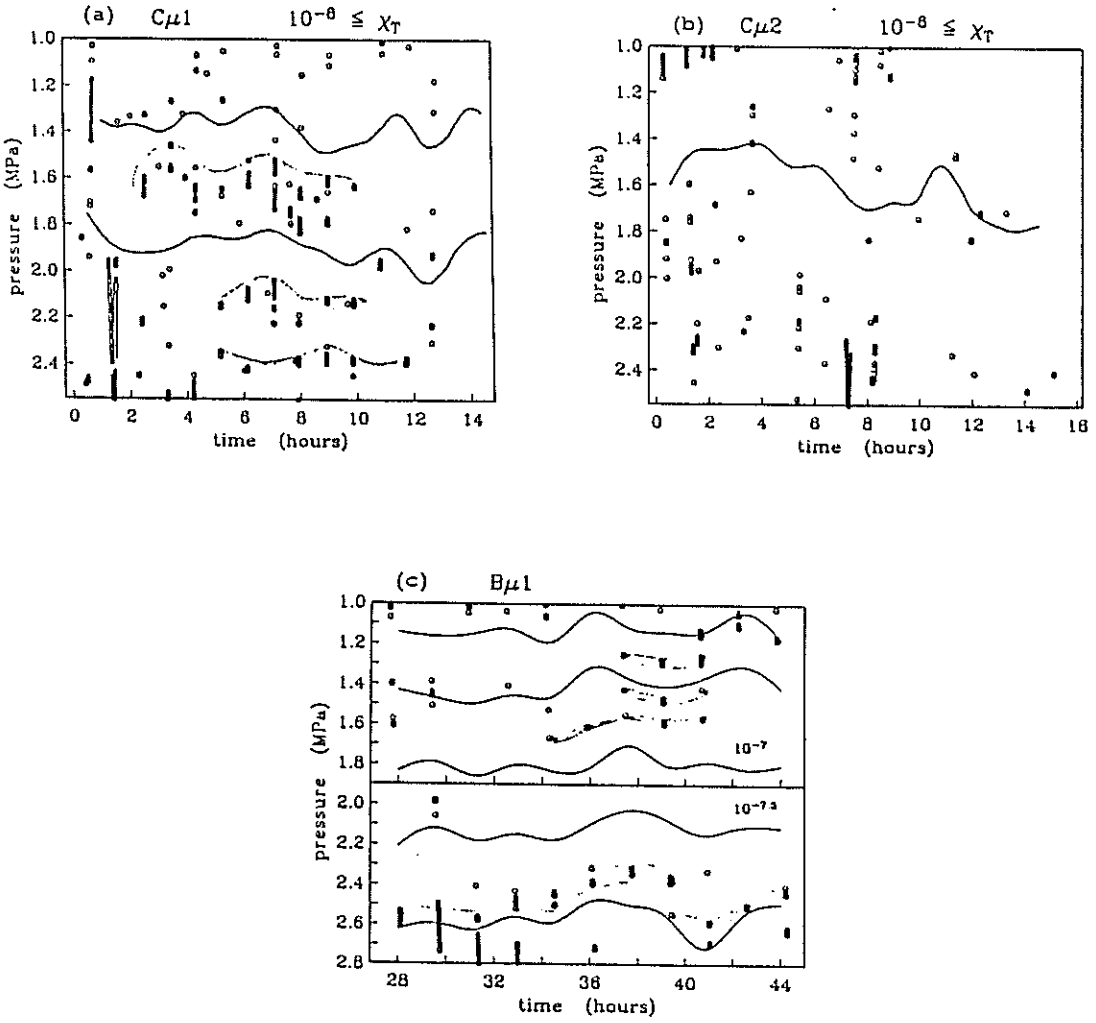

Figure 12. Time-depth maps of χ_T values exceeding thresholds indicated in the top of each frame. The variances calculated each 0.5 meter vertically have not been smoothed. The 9.5° and 10° isotherms are shown in the Cμ1 frame (a), and the 9.5° isotherm is shown in the Cμ2 frame (b). For Bμ1 and Cμ1 (frames a and c) persistent microstructure is seen, and regions of high χ_T spanning three consecutive profiles have been highlighted.

supported well by all the various stratification conditions within which the patches existed.

One explanation is that persistent high χ_T regions contained *TS* steps of the double-diffusive layering type. Steps of this type measured off California by Gregg and Cox (1972) had characteristic magnitudes of about 50 millidegree and 0.015 ppt, and would produce a flat conductivity gradient spectrum with variance 7×10^{-4} $(\mathrm{S\,m^{-2}})^2$ ($\chi_T \approx 7 \times 10^{-8}$ $\mathrm{K^2 s^{-1}}$), consistent with our measurements. The second explanation is that the regions were patches of persistent salt-fingering. Marmorino (1987a) measured regions of salt-fingering with χ_T from [0.4 to 6] $\times 10^{-8}$ $\mathrm{K^2 s^{-1}}$, also consistent with our signal levels. Persistent layers seem more plausible than persistent fingers, which might be destroyed by shear (Kunze, 1987). However, the patches were not in general located at the tops of temperature inversions, where layering is most likely. Of course, the patches in Cμ1 are broad enough vertically so that a combination of fingering and layering is a possibility.

The third explanation is that the patches are caused by the increased likelihood of shear instability, either from reduced stratification or increased shear. Yamazaki and Lueck (1987) show similar persistent patches, and suggest that steady intrusive shear may interact with randomly occurring shear from waves, with this effect dominating microstructure generation even in intrusions susceptible to double-diffusive flux. However, our patches correlated poorly with meter-scale temperature inversions, which mark intrusive flow. Also, our 0.5 meter resolution temperature profiles did not show correlation of weak vertical temperature gradient and persistent patches, although unresolved regions of weak stratification may have existed within a region of apparently stronger stratification based on our course temperature resolution (see for example the high resolution measurements of Gregg and Cox, 1972). The Bμ1 data show little CGV in the [100-200] cpm band (Fig. 10) indicating little salinity variance, and show weak temperature stratification at the layer locations, giving some support for the shear instability explanation.

We believe that temperature microstructure in the Cμ2 sampling volume was mostly due to turbulent overturning, due to the high V, as in the turbulent region of Gregg et al. (1986) and the short lifetimes of high χ_T puffs. Under the mechanical overturning assumption, we can estimate vertical turbulent heat flux in that volume.

6. Application of a turbulent heat flux model to the Cμ2 volume

Continuously acting heat sources are required to maintain a statistically stationary field of temperature fluctuations. We consider the surface region to act as this source in the ocean thermocline. For a steady, locally homogeneous field with $\partial T_0/\partial x_n$ constant, where n indicates the direction normal to the mean isotherms (which we consider to lie horizontally), introduction of a Fickian eddy thermal diffusivity defined by

$$<T'U_n> = -\kappa_e \frac{\partial T_0}{\partial x_n} \tag{4}$$

leads to

$$\overline{\chi}_T = 2\kappa_e \left(\frac{\partial T_0}{\partial x_n} \right)^2 \tag{5}$$

(Tatarski, 1961; Osborn and Cox, 1972). This relation is similar to the definition of $\overline{\chi}_T$, with the mean of true temperature gradients replaced by the mean temperature gradient and κ_T replaced by κ_e. Combining (5) with (3) and disregarding Γ gives

$$C_T = \kappa_e / \kappa_T \tag{6}$$

with heat flux

$$Q = \rho C_p \kappa_T C_T (\partial T_0 / \partial x_n). \tag{7}$$

Tatarski (1961) applied these expressions to atmospheric turbulence, while Osborn and Cox (1972) showed in detail that they can be true for vertical heat flux in the ocean. Gargett (1984) and Gregg (1984, 1987) also discussed this model. Washburn (1987) showed that the assumption of horizontal homogeneity was valid in a volume of water off of southern California and used this volume averaging technique. For calculation we set the specific heat C_p constant at 3980 $\mathrm{J\,kg^{-1}\,K^{-1}}$, and the density ρ constant at 1030 $\mathrm{kg\,m^{-3}}$.

We estimated C_T and Q for averaging volumes of 40 meters depth by 9 $\mathrm{km^2}$. This size is clearly large compared with eddy size of vertical mixing processes, a requirement for the statistical model. There is no evidence in Fig. 12 of time dependence, so averaging the Diver data in time allows expansion of the sample volume and decreases the variance of estimated parameters. Values of $\partial T_0/\partial z$ and C (estimates of C_T) calculated over 0.4 MPa (40 m) intervals for the duration of each experiment were presented in the previous section. Values of $\partial T_0/\partial z$ were determined from T_0 profiles (Fig. 4) made by time averaging T at specific pressures, rather than vice-versa, a procedure which smooths fine structures. Fig. 13 shows the resultant C values from both types of $\overline{\chi}_T$ estimates of the previous section. Table 3 and Fig. 14 show the resultant Q values. The C (or κ_e) have their greatest uncertainty in the shallowest bin, since the two estimates differ greatly. The confidence intervals of C_{mle} coincide with those of $\overline{\chi}_T$ discussed previously, while the confidence intervals for C_{sm} are uncertain because the pdf's of χ_T are clearly not normal.

Since N was approximately constant at pressures greater than 1.0 MPa, the $\kappa_e \propto N^{-1}$ or $\kappa_e \propto N^{-\frac{1}{2}}$ parameterizations of Gargett and Holloway (1984) predict constant C below 1.0 MPa. The slightly higher C between 1.0 to 1.4 MPa disagree with this prediction, but these C are not reliable enough to be conclusive. The average of the two types of Q estimates decreases with depth, and the decrease with depth at pressures greater than 1.0 MPa reflects the disagreement with theory.

Table 3. Vertical turbulent heat flux estimated using the simple one-dimensional turbulent diffusion model.

set	pressure	Q_{mle}	Q_{em}
	MPa	$W m^{-2}$	$W m^{-2}$
Cμ2	0.6-1.0	8.7	0.75
	1.0-1.4	2.0	1.2
	1.4-1.8	0.71	0.41
	1.8-2.2	0.55	0.45

Table 4. Finestructure quantities and dimensionless microstructure parameters C_{em} and C_{mle} for the Cμ2 data set, which has sporadic microstructure.

set	depth	$N_A^2 \times 10^5$	$\overline{\partial_z^2 U} \times 10^5$	R_A	C_{em}	C_{mle}
	MPa	sec^{-2}	sec^{-2}			
Cμ2	0.6-1.0	8.3	8.9	0.93	26	303
	1.0-1.4	1.3	2.7	0.48	268	446
	1.4-1.8	1.5	2.9	0.51	79	137
	1.8-2.2	1.5	1.5	1.0	88	106
	2.2-2.6	1.5	1.7	0.87	-	-

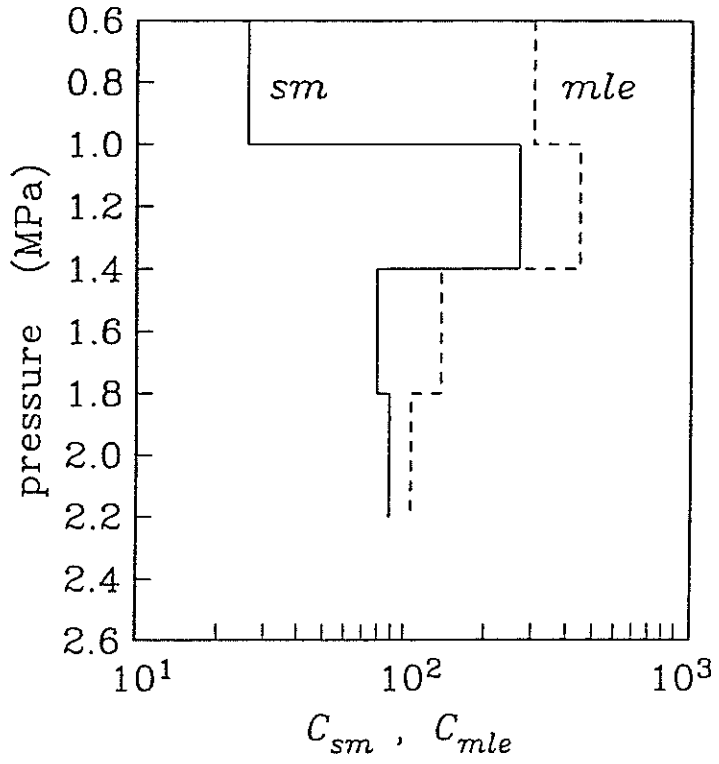

Figure 13. Parameters C_{sm} (sample mean technique) and C_{mle} (maximum-likelihood mean technique) for the Cμ2 sampling volume, calculated for 40-m thick averaging volumes. The value $C = 71$ is equivalent to $\kappa_t = 1 \times 10^{-6}$ m^{2}s^{-1} in the heat flux model.

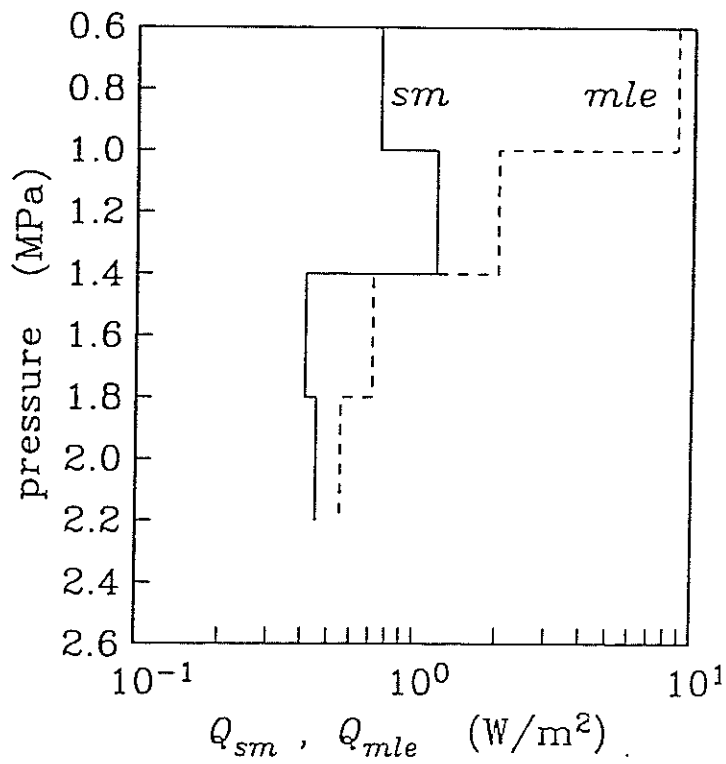

Figure 14. Heat flux estimates for the Cμ2 deployment, as a function of depth, calculated using the C of Figure 13 and mean temperature gradients from Figure 4. The values from 1.0 to 2.2 MPa, a region free of temperature inversions (except at the lowest pressures for the first three profiles (Duda, 1986)) with sporadic microstructure, show agreement within a factor of 2 between the two C estimation techniques.

For the Cμ2 volume, the mean κ_ρ from the maximum-likelihood technique was 3.5×10^{-5} m^{2}sec^{-1}, while the mean κ_ρ from the sample-mean technique was 1.6×10^{-5}. Mean downward heat flux was 1.8 W m^{-2}. Despite the qualitative difference between the microstructure of Bμ1, Cμ1 and Cμ2, the model gives comparable values of κ_ρ and Q for all three volumes. For all three, the mean κ_ρ from the maximum-likelihood technique was 2.5×10^{-5} m^{2}sec^{-1}, while the mean κ_ρ from the sample-mean technique was 3.4×10^{-5}. For all three volumes, downward heat flux averaged 1.9 W m^{-2}.

7. Relation of microstructure and shear in the Cμ2 volume

Since T and U data collected by the Diver during the C experiments (Figs. 5 and 7), we can compare χ_T, C estimates, and gradient Richardson number (Ri) estimates. Individual Ri and χ_T estimates showed no correlation, perhaps due to the limited number of samples (10^4), to noise in the shear measurement, or to an expected time lag between shear and turbulence. Dimensionless mean dissipation C were inversely correlated with volume averaged Ri estimates, but not convincingly. The mean dissipation rate $\overline{\chi}_T$, however, agrees well with that predicted by Henyey et al. (1986) from simulations of strongly interacting internal waves.

The lack of correlation between individual Ri and χ_T is similar to Marmorino et al.'s (1986) lack of correlation between individual C and Ri. As in that paper, $Ri = N^2 / \partial_z^2 U$ was calculated using only the influence of temperature on buoyancy frequency N. A reliable temperature-salinity relation would enable salinity contributions to N to be estimated, giving better Ri estimates. However, variable TS relations in the near-shore region make use of climatic TS little or no better than the disregarding of salinity, so the latter technique is used. Squared vertical shear was calculated $\partial_z^2 U = < \partial U_x / \partial z >^2 + < \partial U_y / \partial z >^2$. Velocities sampled each 0.5 m vertically are block averaged over 10 m for this calculation, indicated by the brackets, the scale-length chosen by D'Asaro (1985) for Ri calculation. The lack of correlation may be due to limitations in our density and shear measurements or to the limited quantity of the measurements.

We also investigated correlation between mean values of Ri and χ_T. Volume averaged Richardson number is defined $Ri_A \equiv N_A^2 < \partial_z^2 U >^{-1}$. The brackets indicate averaging of all 10 m shear values within the 0.4 MPa range. Values are listed in Table 4. The N_A are buoyancy frequency estimates associated with the temperature gradients listed in Table 1, defined $N_A^2 \equiv \alpha g (\partial T_0 / \partial z)$, where α is the expansion coefficient and g is gravitational acceleration. We chose this smoothed stratification estimate because internal waves greater than 10 meters should feel a smoothed version of the density field. In any case, N_A does not vary much from N^2 calculated over 10 m vertical intervals. Error in N_A^2 is estimated at $\pm 10\%$ and square shear error is estimated at 10^{-6}sec^{-1}, giving Ri_A error of about 10%. The sub-unity values of Ri_A suggest that shear instability may have been a microstructure production mechanism.

Considering the uncertainty, Fig. 15 shows no correlation of C and Ri_A, although a trend toward higher C at lower Ri_A is suggested.

Despite the uncertain C to Ri relation, we evaluated whether a model of energy-dependent internal-wave decay predicts our measured levels of microstructure. For a WKB scaled, Garrett-Munk (GM) type internal wave spectrum, the internal-wave decay model of Henyey et al. (1986) predicts the mean kinetic energy dissipation rate from breaking internal waves

$$\overline{\epsilon} = K E^2 N^2 \tag{8}$$

where K is a coefficient composed of other parameters and E is the dimensionless GM energy level. The energy levels in the band from 150 to 15 meters vertical wavelength from the profiles of Fig. 7 are virtually identical for the two sides of the front, 4.2×10^{-3} J kg^{-1}. These are approximately 2.5 times the GM model (Munk, 1981) internal-wave energy for this wavenumber band (Duda, 1986). If we take all GM parameters except E equal to those in Munk (1981), then E is 2.5 times that in Munk (1981) and K is unchanged from that used by Henyey et al. (1986).

We estimated predicted $\overline{\chi}_T$ from predicted $\overline{\epsilon}$ using two methods. One method used the empirical formula $\chi_T = -1.9 \times 10^{-9} + 6.4\epsilon$ of Gregg et al. (1986) (with χ_T in K^{2}s^{-1} and ϵ in W kg^{-1}), measured in the California current. This method predicts that C_T and κ_ϵ scale as N^{-2}. Alternatively, using an expression for the diapycnal turbulent diffusivity of density from Osborn (1980) and setting this equal to κ_ϵ for temperature, one arrives at

$$\chi_T = \left[\frac{2\gamma}{N^2} \left(\frac{\partial T_0}{\partial z} \right)^2 \right] \epsilon \tag{9}$$

where γ is the mixing efficiency, which we set to 0.2 (Osborn, 1980; Gregg et al., 1986; Oakey, 1985). This expression is valid under the above equality assumption and the assumptions required for the turbulent flux model, and predicts that C_T and κ_ϵ are independent of N. The $\kappa_\epsilon \propto N^0$ and $\kappa_\epsilon \propto N^{-2}$ relations suggested here differ from those predicted by Gargett and Holloway (1984), which are $\kappa_\epsilon \propto N^{-1}$ and $\kappa_\epsilon \propto N^{-\frac{1}{2}}$.

For the region of Cμ2 deeper than 1.0 MPa, mean gradient $\partial T_0/\partial z \approx .010$ K m^{-1} gives N approximately 2.4 cph, with resultant $\overline{\epsilon} = 1.3 \times 10^{-9}$ W kg^{-1}. The empirical relation then gives $\overline{\chi}_T = 7 \times 10^{-9}$ K^{2}s^{-1}. The second method yields $\overline{\chi}_T = 5 \times 10^{-9}$. These predicted $\overline{\chi}_T$ values are in good agreement with the Cμ2 $\overline{\chi}_T$ values in Table 1. Note that the predicted and observed values also agree for the Cμ1 volume.

Measured $\overline{\chi}_T$ from the shallower 0.6 to 1.0 MPa regions also show relative agreement with the theory. For the shallow Cμ1 region, the predictions are $\overline{\chi}_T = 1.5 \times 10^{-8}$ (empirical formula) and 2×10^{-8} K^{2}s^{-1} (expression 9), close to the measured values. For the shallow Cμ2 region, the predictions are $\overline{\chi}_T = 4.0 \times 10^{-8}$ (empirical formula)

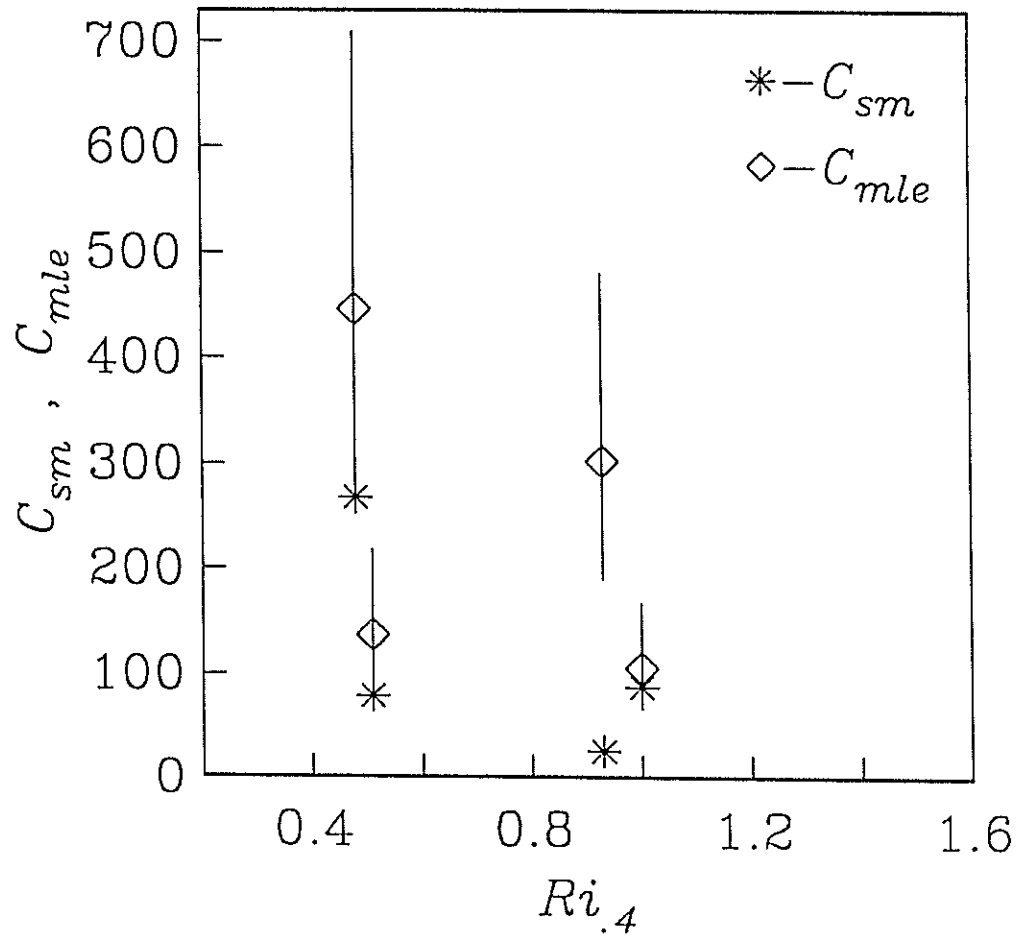

Figure 15. Parameters C_{sm} and C_{mle} plotted versus mean Richardson number estimated over 0.4 MPa averaging volumes. Only values for the Cμ2 deployment with high-V, sporadic microstructure are shown. The 95% confidence intervals shown for the maximum-likelihood estimates assume that only one in four of the 0.005 MPa interval χ_T values are independent (section 5).

and 1.2×10^{-7} $K^2 s^{-1}$ (expression 9). The two estimates of experimental $\overline{\chi}_T$ differ considerably, and bracket the predictions. The shallow $C\mu 2$ region has $V = 9.2$, the highest we have measured, so the sample mean may be an underestimate, according to the analysis of Baker and Gibson (1987).

8. Summary

Profiles of fine scale and microscale quantities have been collected in regions below the surface mixing layer with the quasi-Lagrangian Cartesian Diver. Using measurements of conductivity gradient variance in the band [3-200] cpm we have estimated rates of thermal variance dissipation χ_T. Individual χ_T were found to correlate poorly with individual shear and Richardson number estimates. Patches of χ_T persistently high for many hours were measured and may have been due to sustained double-diffusive activity, since shear and Richardson number were not steadily conducive to shear instability at the patch location. Fine scale stratification parameters were not measured well enough to verify double-diffusion, however.

Since χ_T was measured throughout hourly round-trip profiles we could estimate $\overline{\chi}_T$ in layers within three 160-meter by 9-km^2 'pancake' volumes. One volume, labeled $C\mu 2$, had highly sporadic χ_T, justifying the assumption that χ_T was due to overturning, while two had unexplained persistent microstructure patches. Assuming $\overline{\chi}_T$ and mean vertical temperature gradients to be steady-state, and assuming temperature fluctuation characteristics to be both steady-state and horizontally homogeneous, we estimated of eddy diffusivity of heat κ_e within the volume of sporadic activity. Average κ_e was about 2.5×10^{-5} $m^2 sec^{-1}$, a value comparable to previous estimates.

Mean $\overline{\chi}_T$ within the $C\mu 2$ volume compare well with predictions based on our fine scale temperature and shear observations and the internal-wave decay model of Henyey et al. (1986). Horizontal baroclinic velocity kinetic energy was 4.2×10^{-3} $J\,kg^{-1}$, 2.5 times the Garrett-Munk level, giving predicted mean χ_T from 5 to 120×10^{-9} $K^2 s^{-1}$ for various depth intervals in the thermocline, similar in many cases to our measured values. One method of computing mean χ_T from the internal-wave decay model uses a linear empirical relation between χ_T and ϵ measured by Gregg et al. (1986) to predict $\kappa_e \propto N^{-2}$, while another method predicts κ_e independent of N. We qualitatively agree with each of these because of limitations in our mean χ_T estimates and because of the narrow range of sampled N, and we are unable to distinguish between them.

APPENDIX

Estimation of χ_T with the Cartesian Diver Microconductivity Probe

Our measurement of χ_T with the small four-electrode conductivity probe is subject to three types of error. Error is introduced by the rolloff in spatial response of the cell at about 100 cpm wavenumber. Another source of error is the contribution of salinity fluctuations to conductivity gradient. The final source of error is the small number of spectral bands (six).

Disregarding the limited number of spectral bands, limits of the ratio of estimated $\hat{\chi}_T$ to actual χ_T can be calculated for any combination of ocean parameters ϵ, χ_T and large-scale temperature - salinity relation $|\Delta T/\Delta S|$. The one-dimensional spectrum of sub-meter scale conductivity gradient fluctuations is defined as

$$<(\nabla\sigma)^2> \equiv \int F_{\sigma\sigma}(k)dk \quad . \tag{A1}$$

Expanding conductivity fluctuations $\Delta\sigma = a\,\Delta T + b\,\Delta S$ gives

$$<(\nabla\sigma)^2> = a^2\int F_{TT}(k)dk + b^2\int F_{SS}(k)dk + 2ab\int F_{TS}(k)dk \quad , \tag{A2}$$

where F_{TT}, F_{SS} and F_{TS} are the spectra of temperature and salinity gradient fluctuations, and their cross spectrum, respectively. The conductivity gradient spectrum measured by the Cartesian Diver system is $\hat{F}_{\sigma\sigma} = H^2 F_{\sigma\sigma}$ where $F_{\sigma\sigma} = a^2F_{TT} + b^2F_{SS} + 2abF_{TS}$ and where H^2 is the probe spatial response function, $H^2(k) = [1 + (2\pi\tau k)^2]^{-1}$. Parameter τ is set to 1.6×10^{-3} m within the band [3-200] cpm (Washburn and Deaton, 1986) and zero outside that band.

An approximate ratio of estimated to actual χ_T is

$$R = \frac{\hat{\chi}_T}{\chi_T} = \frac{\int_3^{200} \hat{F}_{\sigma\sigma}(k)dk}{a^2\int_3^{\infty} F_{TT}(k)dk}. \tag{A3}$$

To compute R, we assume that F_{TT} and F_{SS} are given by one-dimensional forms of Batchelor (1959) spectra (Gibson and Schwarz, 1963), $F(k,\epsilon,\chi,\kappa,q)$, where κ is the molecular diffusion coefficient of the scalar quantity considered and χ is the rate of its dissipation. The Batchelor spectral parameter is set $q = 3.7$. For salinity, $\kappa_S = 1.3 \times 10^{-9}\mathrm{m}^2\,\mathrm{sec}^{-1}$, and for temperature $\kappa_T = 1.4 \times 10^{-7}\mathrm{m}^2\,\mathrm{sec}^{-1}$. Salinity fluctuation dissipation is given by $\chi_S = \chi_T|\Delta T/\Delta S|^{-2}$ (Gregg, 1984). If $\Delta T/\Delta S$ is fixed, the absolute levels of χ_T or χ_S do not affect this analysis.

If T and S are perfectly correlated at these scales, then

$$F_{TS} = (F_{TT})^{1/2}(F_{SS})^{1/2}. \tag{A4}$$

If T and S are perfectly anticorrelated, then

$$F_{TS} = -(F_{TT})^{1/2}(F_{SS})^{1/2}. \tag{A5}$$

Fig. A1 shows a^2F_{TT}, b^2F_{SS}, $2ab(F_{TT})^{1/2}(F_{SS})^{1/2}$, and $F_{\sigma\sigma}$ for four combinations of ϵ and $|\Delta T/\Delta S|$. The parameters are set $a = 0.0089\,\mathrm{S\,m^{-1}\,K^{-1}}$ and $b = 0.10\,\mathrm{S\,m^{-1}\,ppt^{-1}}$. To relate χ_T to ϵ for the calculation of this figure, we used the empirical relation of Gregg et al. (1986), $\chi_T = -1.9 \times 10^{-9} + 6.4\epsilon$. Table A1 shows R for 24 combinations of ϵ and $|\Delta T/\Delta S|$. The upper number of each pair is the value calculated assuming perfect TS correlation at wavelengths less than 1 meter, while the lower number is the result for perfect anticorrelation. In the ocean, the expected R will be somewhere within these bounds. The relation between large-scale TS correlation and diffusion-scale TS correlation is governed by diffusive and double-diffusive processes and is considered here to be uncertain. However, χ_S and χ_T are assumed to be related as above.

At high ϵ, the finite response of the probe leads to underestimation of χ_T, especially if T and S are anticorrelated at small scales. At low $|\Delta T/\Delta S|$ and ϵ the contribution of salinity to conductivity signals leads to overestimation of χ_T.

The relationship of $|\Delta T/\Delta S|$ to intrusive behavior can be examined with CTD data collected in the C data region in October, 1983 by Washburn and Armi (1987) (Figs. A2 and A3). $|\Delta T/\Delta S|$ is related to the density ratio $R_\rho = \beta\partial_z S/\alpha\partial_z T$, where β and α are the coefficients of haline contraction and thermal expansion, respectively. Strong intrusions will often have R_ρ near -1 ($\Delta T/\Delta S$ near 3.5), until double-diffusion or turbulence smooths out the TS curve. Both diffusive layering and salt fingering processes occur most strongly for R_ρ near -1, with fingering at $R_\rho < -1$ ($\Delta T/\Delta S > \approx 3.5$). Station 1 in a cool offshore jet is free of intrusions, indicated by the smooth TS curve in Fig. A2. Station 10, south of the jet in a region of warmer surface water, has an uneven TS curve often aligned roughly along isopycnal curves, $R_\rho = 1$ (from lower left to upper right) for $T < 9$ degrees, Fig. A3. Histograms of $|\Delta T/\Delta S|$ calculated over roughly two meter vertical intervals are shown in Fig. A4. $|\Delta T/\Delta S|$ less than 2 are situations subject to highest error, Table A1. Fifteen percent of the upper 500 meters at station 10 fit this category; only two percent at station 1.

Fig. 10 shows the ratio of $\hat{\chi}_T$ from the [3-200] cpm band to that from the [3-100] cpm band to exceed 2 a few percent of the time for 1.0-1.4 MPa Cμ1 data. Theoretical values of this ratio are given in Table A2. The combination of $\Delta T/\Delta S$ near -1 and high ϵ is a situation exhibiting this behavior.

The predicted spectra of conductivity gradient (Fig. A1) are of low slope in the band [3-50] cpm, so only the [50-100] cpm and [100-200] cpm bands are subject to error due to changes of spectral density within the band. The energy density is considered to be evenly distributed throughout each band. Therefore χ_T will be slightly overestimated for low values of ϵ at high $|\Delta T/\Delta S|$, a situation where the spectrum falls with increasing wavenumber in the [50-200] cpm region.

Table A1. R values for various ϵ and various large-scale $|\Delta T/\Delta S|$. The upper entry is for perfect TS correlation at sub-meter scales, the lower entry is for perfect anticorrelation. Double-diffusive activity requires positive TS correlation.

	$\epsilon = 10^{-6}$ W m^{-3}	$\epsilon = 10^{-6}$	$\epsilon = 10^{-7}$	$\epsilon = 10^{-8}$
$\|\Delta T/\Delta S\| = 0.6$ K ppt^{-1}	80 64	36 23	15 6.5	6.2 1.6
$\|\Delta T/\Delta S\| = 1$	31 22	15 7.1	7.0 1.7	3.0 0.29
$\|\Delta T/\Delta S\| = 3$	5.4 2.1	3.3 0.63	1.9 0.16	1.00 0.09
$\|\Delta T/\Delta S\| = 6$	2.5 0.81	1.8 0.44	1.2 0.30	0.67 0.21
$\|\Delta T/\Delta S\| = 10$	1.7 0.69	1.3 0.52	0.94 0.41	0.56 0.28
$\|\Delta T/\Delta S\| = 20$	1.2 0.74	1.04 0.65	0.78 0.51	0.48 0.34

Table A2. The ratio of $\hat{\chi}$ estimated using data in the band [3-200] cpm to $\hat{\chi}$ estimated using the [3-100] cpm band. Entries are for the same situations as table A1.

	$\epsilon = 10^{-6}$ W m^{-3}	$\epsilon = 10^{-6}$	$\epsilon = 10^{-7}$	$\epsilon = 10^{-8}$
$\|\Delta T/\Delta S\| = 0.6$ K ppt^{-1}	1.62 1.93	1.68 2.45	1.77 2.83	1.91 2.84
$\|\Delta T/\Delta S\| = 1$	1.54 2.05	1.56 2.95	1.64 4.13	1.82 4.68
$\|\Delta T/\Delta S\| = 3$	1.29 2.36	1.26 3.52	1.39 1.45	1.63 1.13
$\|\Delta T/\Delta S\| = 6$	1.14 1.60	1.33 1.26	1.28 1.05	1.56 1.30
$\|\Delta T/\Delta S\| = 10$	1.07 1.19	1.08 1.05	1.23 1.08	1.52 1.37
$\|\Delta T/\Delta S\| = 20$	1.02 1.04	1.04 1.01	1.19 1.11	1.49 1.41

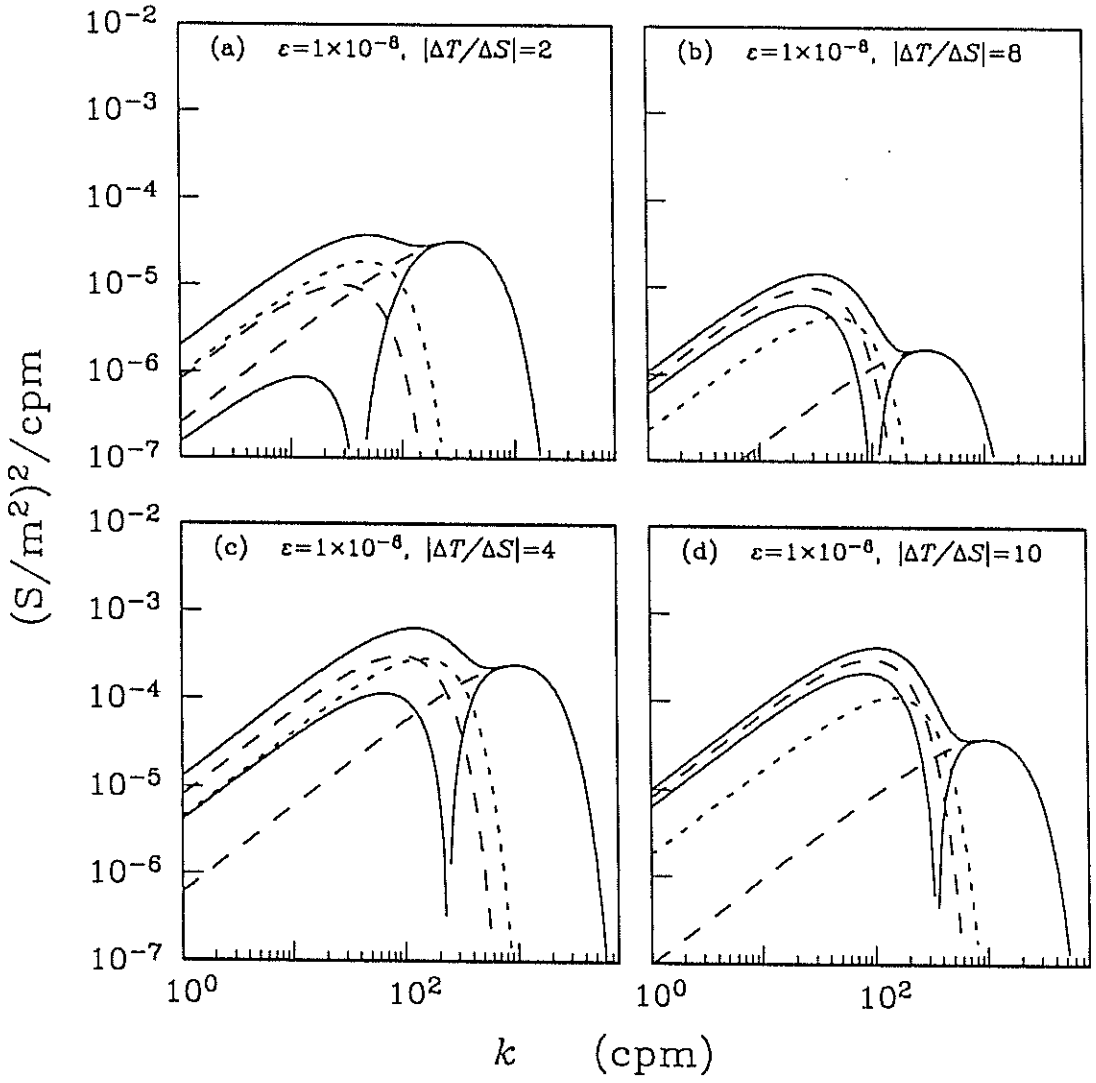

Figure A1. Conductivity gradient spectra for example ϵ and TS relations, along with components of the spectrum as in (A2). The long-dashed curves (a^2F_{TT} and b^2F_{SS}) are related to Batchelor spectra of T and S, the dotted curves are cross spectra abF_{TS}. The solid lines are conductivity gradient spectra $F_{\sigma\sigma}$, which are the formed by adding the dashed curves and either adding or subtracting the dotted curve. The lower solid line is for anticorrelated T and S (subtract cross spectrum), the top is for correlated T and S.

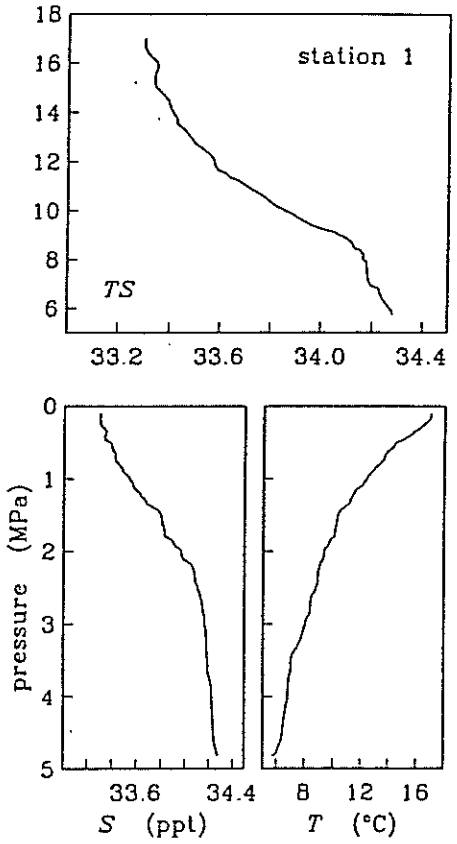

Figure A2. CTD T and S data from a station of Washburn and Armi (1987) near the location of the C deployments.

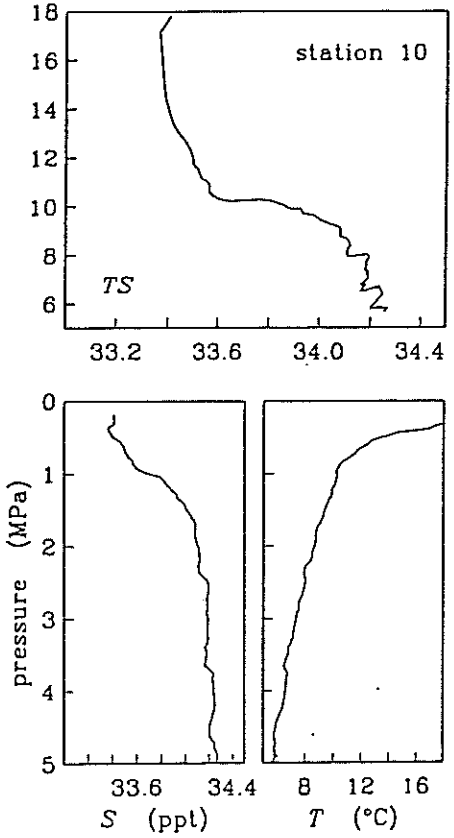

Figure A3. Similar to Figure A2, for a different but nearby station.

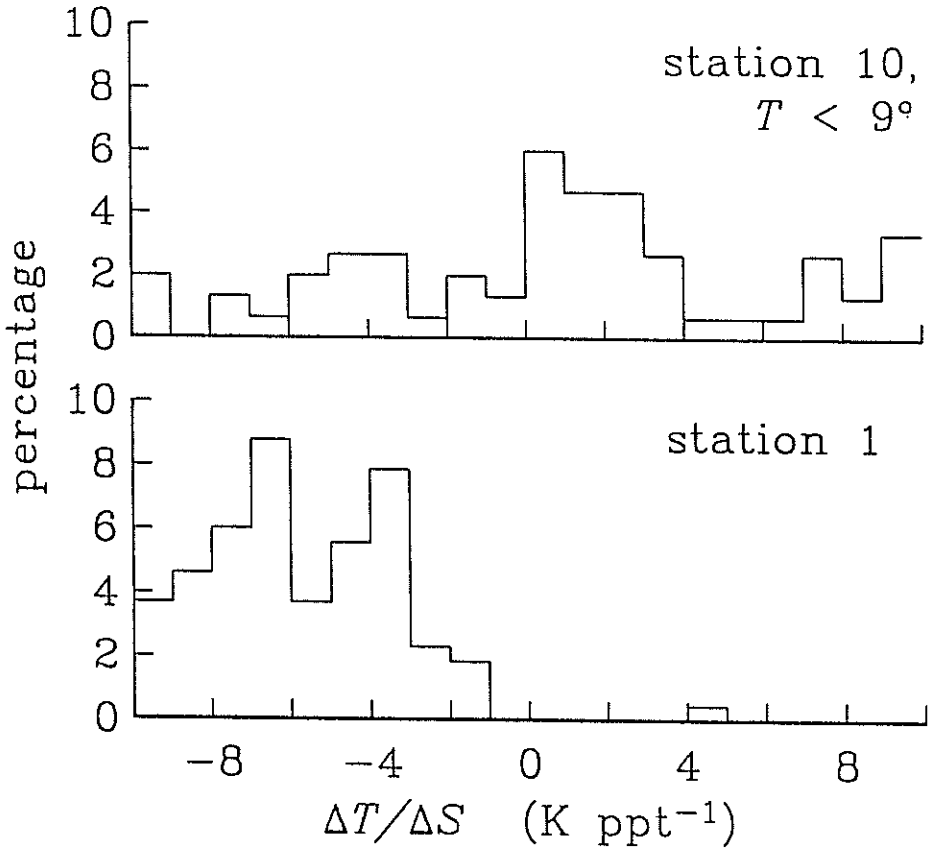

Figure A4. Histograms of TS relation for two meter intervals, from data of Figs. A2 and A3. In each case $\Delta T/\Delta S > 10$ for fifty percent of the samples, so that the percentages do not sum to 100.

REFERENCES

Baker, M. A., and C. H. Gibson, 1987: Sampling turbulence in the stratified ocean: Statistical consequences of strong intermittency. *J. Phys. Oceanogr.*, **17**, 1817-1836.

Batchelor, G.K., 1959: Small-scale variation of convected quantities like temperature in turbulent fluid: Part 1. General discussion and the case of small conductivity. *J. Fluid Mech.*, **5**, 113-133.

D'Asaro, E. A., 1985: Upper ocean temperature structure, inertial currents, and Richardson numbers observed during strong meteorological forcing. *J. Phys. Oceanogr.*, **15**, 943-962.

Desaubies, Y. J. F., and W. K. Smith, 1982: Statistics of Richardson number and instability in oceanic internal waves. *J. Phys. Oceanogr*, **12**, 1245-1259.

Dillon, T. M., and M. M. Park, 1987: The available potential energy of overturns as an indicator of mixing in the seasonal thermocline. *J. Geophys. Res.*, **92**, 5345-5353.

Duda, T. F., 1986: Observations of horizontal flow, vertical shear and microstructure in the upper ocean. Ph.D. dissertation, University of California at San Diego.

Duda, T. F., and C. S. Cox, 1987: Vorticity measurement in a region of coastal ocean eddies by observation of near-inertial oscillations. *Geophys. Res. Lett.*, **14**, 793-796.

Duda, T. F., C. S. Cox and T. K. Deaton, 1988: The Cartesian Diver: A self-profiling Lagrangian velocity recorder. *J. Atmos. Ocean. Tech.*, **5**, 16-33.

Elliott, J. A., and N. S. Oakey, 1980: Average microstructure levels and vertical diffusion for Phase III, GATE. *Deep-Sea Res.*, **26**(GATE Supplement I), 279-294.

Gargett, A. E., 1984: Vertical eddy diffusivity in the ocean interior. *J. Mar. Res.*, **42**, 359-393.

Gargett, A. E., and G. Holloway, 1984: Dissipation and diffusion by internal wave breaking. *J. Mar. Res.*, **42**, 15-27.

Gibson, C. H. 1987: Fossil turbulence and intermittency in sampling oceanic mixing processes. *J. Geophys. Res.*, **92**, 5383-5404.

Gibson, C. H., and W. H. Schwarz, 1963: The universal equilibrium spectra of turbulent velocity and scalar fields. *J. Fluid Mech.*, **16**, 365-384.

Gregg, M. C., 1977: Variations in the intensity of small-scale mixing in the main thermocline. *J. Phys. Oceanogr.*, **7**, 436-454.

Gregg, M. C., 1984: Entropy generation in the ocean by small-scale mixing. *J. Phys. Oceanogr.*, **14**, 688-711.

Gregg, M. C., 1987: Diapycnal mixing in the thermocline: A review. *J. Geophys. Res.*, **92**, 5249-5286.

Gregg, M. C., and C. S. Cox, 1972: The vertical microstructure of temperature and salinity. *Deep-Sea Res.*, **19**, 355-376.

Gregg, M. C., E. A. D'Asaro, T. J. Shay and N. Larson, 1986: Observations of persistent mixing and near-inertial internal waves. *J. Phys. Oceanogr.*, **16**, 856-885.

Henyey, F. S., J. Wright and S. M. Flatté, 1986: Energy and action flow through the internal wave field: An eikonal approach. *J. Geophys. Res.*, **91**, 8487-8496.

Kosro, P. M., and A. Huyer, 1986: CTD and velocity surveys of seaward jets off northern California, July 1981 and 1982. *J. Geophys. Res.*, **91**, 7680-7690.

Kunze, E., 1987: Limits on growing, finite-length salt fingers: A Richardson number constraint. *J. Mar. Res.*, **45**, 533-567.

Marmorino, G. O., 1987a: Observations of small-scale mixing processes in the seasonal thermocline. Part I: Salt fingering. *J. Phys. Oceanogr.*, **17**, 1339-1347.

Marmorino, G. O., 1987b: Observations of small-scale mixing processes in the seasonal thermocline. Part II: Wave breaking. *J. Phys. Oceanogr.*, **17**, 1348-1355.

Marmorino, G. O., L. J. Rosenblum, J. P. Dugan and C. Y. Shen, 1985: Temperature fine-structure patches near an upper-ocean density front. *J. Geophys. Res.*, **90**, 11,799-11810.

Marmorino, G. O., J. P. Dugan and T. E. Evans, 1986: Horizontal variability of microstructure in the vicinity of a Sargasso Sea front. *J. Phys. Oceanogr.*, **16**, 967-980.

Moum, J. N., and T. R. Osborn, 1986: Mixing in the main thermocline. *J. Phys. Oceanogr.*, **16**, 1250-1259.

Munk, W. H., 1966: Abyssal recipes. *Deep-Sea Res.*, **13**, 707-730.

Munk, W. H., 1981: Internal waves and small scale processes. *Evolution of Physical Oceanography*, B. A. Warren and C. Wunsch, Eds., The MIT Press, 264-290.

Oakey, N., 1985: Statistics of mixing parameters in the upper ocean during JASIN phase 2. *J. Phys. Oceanogr.*, **15**, 1662-1675.

Osborn, T. R., and C. S. Cox, 1972: Oceanic fine structure. *Geophys. Fluid Dyn.*, **3**, 321-345.

Osborn, T. R., and R. Lueck, 1985: Turbulence measurements with a submarine. *J. Phys. Oceanogr.*, **15**, 1502-1520.

Tatarski, V. I., 1961: *Wave Propagation in a Turbulent Medium*, McGraw-Hill Book Company, 285 pp.

Washburn, L., and C. H. Gibson, 1982: Measurements of oceanic temperature microstructure using a small conductivity sensor. *J. Geophys. Res.*, **87**, 4230-4240.

Washburn, L., and C. H. Gibson, 1984: Horizontal variability of temperature microstructure at the base of a mixed layer during MILE. *J. Geophys. Res.*, **89**, 3507-3522.

Washburn, L., and L. Armi, 1987: Observations of frontal instabilities on an upwelling filament, in press.

Washburn, L., and T. K. Deaton, 1986: A simple system for mapping conductivity microstructure. *J. Atmos. Ocean. Tech.*, **3**, 345-355.

Washburn, L, 1987: Two-dimensional observations of temperature microstructure in a coastal region. *J. Geophys. Res.*, **92**, 10,787-10,798.

Yamazaki, H., and R. Lueck, 1987: Turbulence in the California undercurrent. *J. Phys. Oceanogr.* **17**, 1378-1396.